



LAWRENCE  
LIVERMORE  
NATIONAL  
LABORATORY

# Graphite Resistive heated Diamond Anvil Cell for simultaneous high-pressure and -temperature diffraction experiments

H. Hwang, Y. Bang, J. Choi, H. Cynn, Z. Jenei, W. J. Evans, A. Ehnes, I. Schwack, K. Glazyrin, G. D. Gatta, P. Lotti, C. Sanloup, Y. Lee, H. P. Liermann

September 30, 2023

Review of Scientific Instruments

## **Disclaimer**

---

This document was prepared as an account of work sponsored by an agency of the United States government. Neither the United States government nor Lawrence Livermore National Security, LLC, nor any of their employees makes any warranty, expressed or implied, or assumes any legal liability or responsibility for the accuracy, completeness, or usefulness of any information, apparatus, product, or process disclosed, or represents that its use would not infringe privately owned rights. Reference herein to any specific commercial product, process, or service by trade name, trademark, manufacturer, or otherwise does not necessarily constitute or imply its endorsement, recommendation, or favoring by the United States government or Lawrence Livermore National Security, LLC. The views and opinions of authors expressed herein do not necessarily state or reflect those of the United States government or Lawrence Livermore National Security, LLC, and shall not be used for advertising or product endorsement purposes.

# **Graphite Resistive heated Diamond Anvil Cell for simultaneous high-pressure and -temperature diffraction experiments**

Huijeong Hwang<sup>1,2,\*</sup>, Yoonah Bang<sup>3,#</sup>, Jinhyuk Choi<sup>3</sup>, Hyunchae Cynn<sup>4</sup>, Zsolt Jenei<sup>4</sup>, William J. Evans<sup>4</sup>, Anita Ehnes<sup>1</sup>, Iris Schwark<sup>1</sup>, Konstantin Glazyrin<sup>1</sup>, G. Diego Gatta<sup>5</sup>, Paolo Lotti<sup>5</sup>, Chrystèle Sanloup<sup>6</sup>, Yongjae Lee<sup>3</sup>, Hanns-Peter Liermann<sup>1</sup>

<sup>1</sup>Deutsches Elektronen-Synchrotron DESY, Notkestr. 85, 22607 Hamburg, Germany

<sup>2</sup> School of Earth Sciences and Environmental Engineering, Gwangju Institute of Science and Technology, 123 Cheomdan-Gwagiro, Gwangju 61005, Republic of Korea

<sup>3</sup>Earth System Sciences, Yonsei University, 50 Yonsei-ro, Seodaemun-gu, Seoul 03722, Republic of Korea

<sup>4</sup>Lawrence Livermore National Laboratory, 7000 East Avenue, Livermore, CA 94550, USA

<sup>5</sup>Dipartimento di Scienze della Terra 'Ardito Desio', Università degli Studi di Milano, Via Botticelli 23, Milan 20133, Italy

<sup>6</sup>Institut de Minéralogie, de Physique des Matériaux et de Cosmochimie (IMPMC), Sorbonne Université, Muséum National d'Histoire Naturelle, UMR CNRS 7590, IRD UR206, 75005 Paris, France

<sup>#</sup>Present address: Korea Atomic Energy Research Institute (KAERI), Daedeok-daero 989 beon-gil, Daejeon 34057, Republic of Korea

\*Corresponding Author: Huijeong Hwang (huijeonghwang@gist.ac.kr)

## **Abstract**

High pressure and temperature experiments using a resistively heated diamond anvil cell have the advantage of heating samples homogeneously with precise temperature control. Here, we present the design and performance of a graphite resistive heated diamond anvil cell (GRHDAC) setup for powder and single crystal X-ray diffraction experiments developed at the Extreme Conditions Beamline (P02.2) at PETRA III, Hamburg, Germany. In the GRHDAC, temperatures up to 2000 K can be generated at high-pressures by placing the GRHDAC in a water-cooled vacuum chamber. Temperature estimates from thermocouple measurements are within  $\pm 35$  K at the sample position up to 800 K and within  $\pm 90$  K between 800-1400 K when using a standard seat combination of cBN and WC. Isothermal compression at high-temperature can be achieved by employing a remote membrane control system. The advantage of the GRHDAC is demonstrated through the study of geophysical processes in the Earth's crust and upper mantle region.

## **Introduction**

Exploring the physical properties of materials at high-pressure and simultaneous high-temperature, by X-ray diffraction at large scale synchrotron radiation facilities, is relevant to understanding the dynamics of the Earth interior<sup>1</sup> as well as in the characterization and synthesis of industrially relevant materials.<sup>2,3</sup> Heated diamond anvil cells (DAC) have been essential for these types of investigation, especially at pressures beyond the current capabilities of large volume press devices,<sup>4,5</sup> i.e. up to 150 GPa and at 2000-3000 K. Heating of the diamond anvil cell can be achieved by means of: a) external or internal electrical resistive heaters, which can reach temperatures up to 2000 K<sup>6</sup> and 3000 K<sup>7</sup>, respectively, and b) infrared laser heating through the transparent diamonds aiming at temperatures between 1200 to 6000 K.<sup>4</sup> Both DAC heating approaches have their advantages and disadvantages. While laser heated DACs can

reach high-pressures and -temperatures (up to 300 GPa and 6000 K), the temperature distribution in the sample is prone to steep temperature gradients. The uncertainty of temperature measurement to below 1200 K is also one of critical limitation of laser heated DACs. By inducing larger area laser heating and probing the sample with a smaller X-ray beam the issue of steep temperature gradient can be minimized but reduces the maximum temperature achievable. Furthermore, infrared laser heating of transparent samples can only be achieved when placing a dark coupler in the chamber adjacent to the sample. However, these metal couplers can induce contamination of and reaction with the sample as well as inhomogeneous heating. Far infrared lasers are slowly being implemented at different synchrotron radiation facilities. They do not require absorbers for transparent materials, have a larger heating spot, but temperature determination in the low temperature regime can still be very challenging. In addition, temporal fluctuations in the heating spot may contribute to the uncertainties in the temperature stability and consequently its estimation. Resistive heated DACs, on the other hand, are limited to lower pressure and temperature regimes, but offer excellent homogenous temperature distribution across the sample and can heat every material stably. There are two types of resistive heated DAC based on the location of the heater: internal and external. In the case of internal resistive heated DACs, the heater takes the form of a metal foil e.g. Re<sup>7</sup> or fine wire and is placed in the sample chamber. As a result, heat is generated only within the sample chamber reaching temperatures up to 3000 K. However, the complexity of the gasket design required to install the insulator and heater in the small sample chamber can make handling of the setup difficult. External resistive heated DACs use heating wires that form a coil and are installed near the diamonds to heat either the entire DAC<sup>8</sup> or just the tip of the diamond anvil.<sup>9-</sup>

<sup>11</sup> In comparison with internal resistive heated DACs, external resistive heated DACs are limited to temperatures of 2000 K and require auxiliary equipment such as water-cooled

vacuum chambers to prevent oxidation of the pressure cell and its components. Nevertheless, external resistive heated DAC is often preferred rather than internal resistive heated DACs due to their simpler preparation including that of the heater. Unfortunately, coil heaters installed around diamond tip either cannot reach high temperatures (above 1100 K) because the wire will eventually melt, or are extremely delicate, so that they easily shear off during heater preparation and pressurization. Thus, there has been a need for a robust externally resistive heated DAC that can reach high temperatures up to 2000 K and that can be employed at high-pressure beamlines for X-ray diffraction studies. Such external resistive heated DAC for powder X-ray diffraction has been developed over the last decade by using flexible<sup>12-15</sup> or rigid graphite sheets<sup>16-17</sup> which are very robust, can easily surround and heat the tip of the diamond anvils as well as the gasket and sample, thus reaching very high-temperatures without oxidation of the DAC components if used within a vacuum chamber. The flexible graphite resistive heated DAC (GRHDAC) has the advantage of directly touching the diamond and thus heating the tip of the diamond, as well as the gasket and the sample, by conductive heat transfer in contrast to the rigid graphite heater. Thus, the graphite heater in the GRHDAC ensures that temperature gradients that might arise from the high thermal conductivity of the diamonds, are minimized because the entire tip of the diamond is heated. The flexible graphite heater has also been used in single crystal X-ray diffraction studies by adapting the GRHDAC with large opening Bohler-Almax seats.<sup>18</sup> The flexible graphite heater has been tested extensively at the Extreme Conditions Beamline P02.2 at PETRA III by heating several internal standards in the GRHDAC to estimate temperature measurement uncertainties resulting from changing positions of the thermocouple junctions with respect to the sample positions. This work describes the GRHDAC setup in detail and its current ability to accurately estimate sample temperatures by comparing temperatures determined from thermocouple readings with those

derived from unit cell volumes and equations of state (EoS) of known standards situated in the sample chamber. Finally, a brief overview of different applications of the GRHDAC is provided as well as an outlook on future developments necessary to further improve the performance of the internal GRHDAC.

## Experimental Method

The GRHDAC consists of four main components: a diamond anvil cell, a direct current (DC) powered electrical heating circuit with thermocouple read out system, a vacuum vessel with water cooling, and a membrane drive system.

### *Design of the GRHDAC*

The GRHDAC is based on a modified 4-pin type DAC developed by the high-pressure group from Lawrence Livermore National Lab (LLNL) to accept flexible graphite sheet heaters.<sup>5</sup> The 4-pin DAC comprises two parts: a main body, and a cup that screws on to the main body from the downstream side securing the membrane between the main body and the cup. The cell is further equipped with a tungsten carbide (WC) seat, with a slit or cone shape opening on the upstream side, and a conical cubic boron nitride (cBN) or Böhler-Almax type seat on the downstream side to perform powder or single crystal X-ray diffraction measurements. A schematic diagram of the GRHDAC is shown in Fig. 1. In the GRHDAC, two pieces of flexible graphite sheets (Alfa Aesar, part 42953, graphite foil, 0.5 mm thick, 99.8%) sandwich a Re gasket. Both the gasket and graphite sheets are indented to ensure tight contact of the graphite sheets with diamond and gasket. Each graphite sheet is pushed against L-shaped molybdenum electrodes that provide electricity from the outside through the DAC walls parallel to the compression axis from the upstream side to the graphite heaters. The Mo electrodes are insulated by alumina sleeves to isolate the electrical circuit from the DAC body. For the same reason, 0.5 mm thick alumina discs with central openings are glued to both seats, which also provide electrical insulation of the flexible graphite sheets (Fig. 1).

### *Electrical Heating and Temperature Measurement System*

R-type thermocouples are employed to monitor the temperature up to 1723 K. They are located on the pavilion of each diamond anvil. The junctions of the thermocouples are fixed approximately 700  $\mu\text{m}$  below the culet edge of each diamond (Fig. 1). After fixing the position of thermocouple junctions on each diamond, the thermocouple junction is covered with cement (RESBOND 989 from Cotronics Corp.) to prevent contact to the graphite heater and gasket. This ensures accurate temperature measurements at the diamond tips to estimate the sample temperature in the gasket. The thermocouple electromotive force (EMF) is transferred to the outside of the vacuum vessel via a feedthrough (CF16-TCL2-CE-RS from VACOM) and read by a multimeter (Keithley 3706A) with a cold junction correction board. Mo rods of the GRHDAC are connected to the outside of the 4-pin DAC by means of copper rods that guide the electrical current to the outside of the vacuum chamber through a high-power electrical feedthrough and high-power welding cables connected to a DC power supply (Fig. 1(C), Agilent 6601, 220 A and 8V). The DC power supply and the thermocouple read out system have been incorporated into the control software of the P02.2 beamline.

### *Vacuum vessel, water cooling and membrane manifold*

In order to prevent heat loss and oxidation of the different components of the GRHDAC during heating, the entire setup is placed inside a customized vacuum-chamber. This chamber consists of a stainless-steel tube positioned in the vertical direction, which is welded shut with ConFlat (CF) vacuum flanges at the bottom and top. The tube has two cutouts at the height of the sample, one circular opening on the downstream side providing  $\pm 45^\circ$  access in  $2\theta$  and a rectangular opening with  $\pm 60^\circ$  access on the upstream side. The openings are sealed with Kapton foil, permitting the X-rays to travel to and from the sample in the DAC without

significant loss of X-ray intensity. The top CF flange has been modified to accept vacuum feedthroughs for the thermocouples (CF16-TCL2-CE-RS from VACOM), electrical power (CF40-HC8-2-CE-CU64 from VACOM), water cooling, and a membrane capillary, as well as a Quick Flange (QF)20 to connect a vacuum pump via a hose. The vacuum reached with a standard pump system from PETRA-III is better than  $1 \times 10^{-4}$  mbar, which is sufficient to prevent oxidation of the heated diamonds and metal components. To protect the sample positioning system underneath the vacuum chamber from heat transfer, the interface plate to the BKL-4 kinematic mount (Newport,) is water cooled, as is the outside of the main cell body of the 4-pin DAC. The pressure on the membrane that compresses sample is remotely controlled using either a pressure controller from Sanchez Technology (APD 200) or from General Electric (GE) (PACE 6000).

#### *Temperature calibration using X-ray diffraction measurement in the GRHDAC*

Estimation of the sample temperature in the GRHDAC can be performed in different ways: a) using thermocouples placed close to the sample chambers or b) using internal X-ray diffraction standards. Because internal standards in the sample chamber may be subjected to reaction and pressure effects, temperature determination using thermocouples during simultaneous high-pressure and -temperature experiment is indispensable for estimating the accurate sample temperature. This approach, however, requires the placement of the thermocouples to be very reproducible, so that temperature gradients are minimal, and prior calibration of the temperature difference between the sample and thermocouple position can be applied to estimate an accurate sample temperature. In order to estimate the temperature difference between the sample and thermocouple position, X-ray diffraction standards (Al, NaCl, and Au) with a known high-temperature EoS were placed in the sample chamber and X-

ray diffraction patterns collected to measure the change of the unit-cell volume as a function of temperature at ambient pressure. Anhydrous NaCl powder with 99.999 % purity from Sigma Aldrich (Product no. 450006), Al and Au foils from Goodfellow were used as standards. The Al foil was separated from Au foil by NaCl powder to avoid the formation of alloys. Some of the X-ray diffraction patterns did not show any diffraction peaks from Al, and hence only diffraction data of NaCl and Au were used to determine the temperature in the sample chamber.

*In-situ* high-temperature and -pressure synchrotron X-ray diffraction measurements were conducted at beamline P02.2 at PETRA-III, Hamburg, Germany. Monochromatic synchrotron X-ray radiation was tuned to an energy of 25.6 keV ( $\lambda = 0.4828(1) \text{ \AA}$ ) with a beam size of 3 (h) x 8 (v)  $\mu\text{m}^2$  full width at half maximum (FWHM) focused by means of compound refractive lenses (CRLs). X-ray diffraction data were collected on a 2-dimensional Perkin Elmer XRD 1621 detector. Calibration of the sample-to-detector distance and detector tilt was performed using a  $\text{CeO}_2$  standard from NIST (SRM 674b) with DIOPTAS,<sup>19</sup> which was also used to convert diffraction images to 1-dimensional  $2\theta$  values plots. All temperature and pressure calibration experiments were performed employing type-*Ia* standard-designed diamonds with 0.3 mm culet size and different seat configurations (see below). X-ray diffraction standards for the temperature calibration were loaded in a pre-indented rhenium gasket with an indentation thickness of 0.03 – 0.04 mm, and a hole of a 0.180 mm in diameter drilled by an electric discharge machine (EDM). X-ray diffraction data were collected after a stabilization period of approximately 10 minutes after reaching the desired temperatures in 50 K intervals. In order to prevent the cell closure that would result in compression of the sample during heating, set screws were engaged.

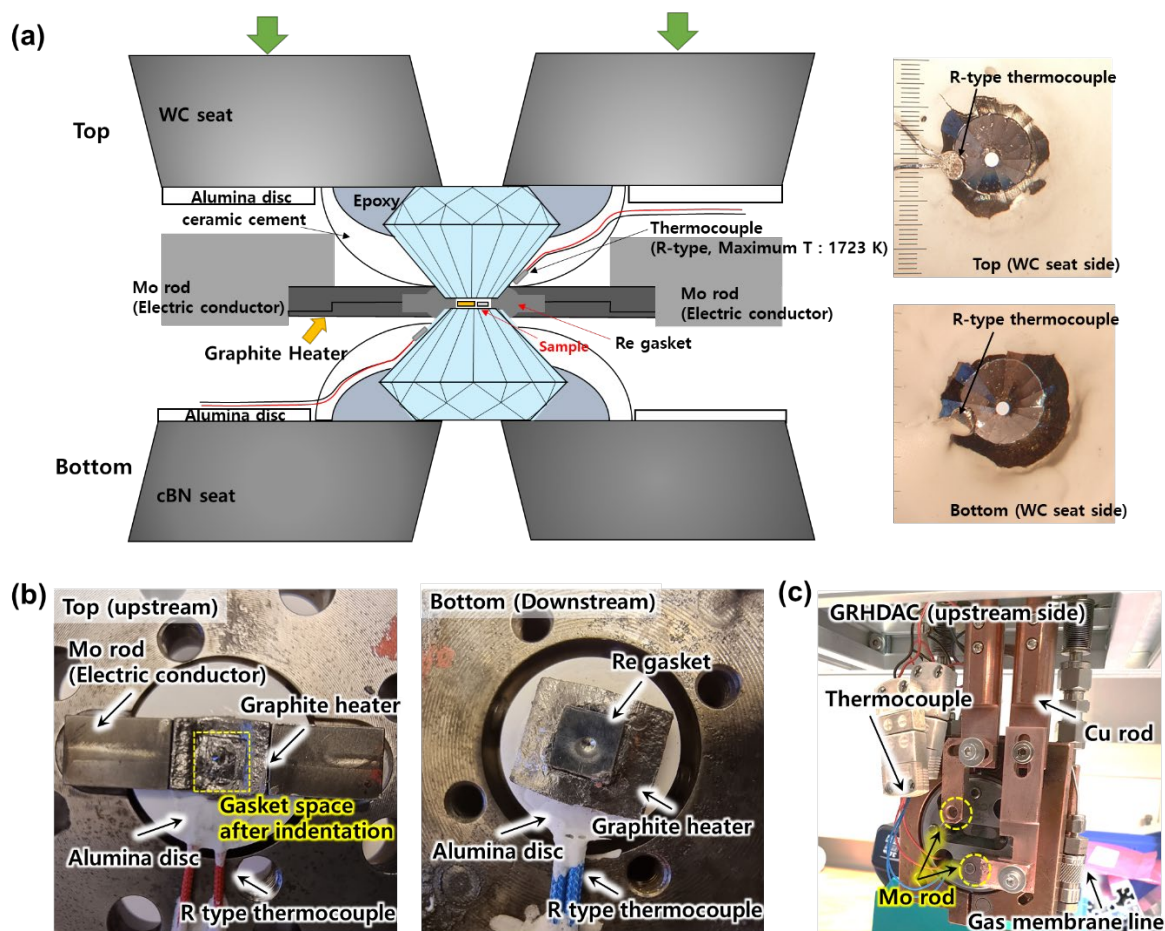


**Fig. 1.** (a) Schematic image of GRHDAC setup (left) and photographs of the anvils (right) indicating the position of the R-type thermocouple on the pavilion of the diamond anvils. (b) Photographs of GRHDAC heater of the WC seat side (left) and cBN seat side (right). (c) Assembly of GRHDAC before placement into the vacuum chamber showing Mo electrodes, thermocouple wires and He gas membrane line.

## Results & Discussion

### A. Thermal expansion of the temperature standards at ambient pressure

Fig. 2 and 3 show the results of two calibration runs performed at ambient pressure. In Fig. 2, we plot the results from the 1<sup>st</sup> calibration run with pure NaCl as an internal standard, up to its melting temperature of 1074 K.<sup>20</sup> Results of the 2<sup>nd</sup> and 3<sup>rd</sup> run with mixed internal standards (Al, NaCl, and Au) are presented in Fig. 3. In both experiments, the temperature of the sample was estimated by determining the unit-cell volume from the diffraction pattern of the standard in conjunction with the thermal EoS of NaCl,<sup>21</sup> and Au<sup>22</sup> at ambient pressure, until the melting of the respective standards.<sup>23</sup> The melting temperatures of the standards were determined by the disappearance of diffraction peaks and the appearance of diffuse scattering signal. Fig. 2(B) and 2(C) indicate that, in 1<sup>st</sup> calibration run, the difference between the temperature of the two thermocouple probes is relatively small (below 10 K) while the difference to the actual sample temperature is below 30 K up to 800 K and below 90 K up to the melting point of NaCl (1074 K). In the 2<sup>nd</sup> and 3<sup>rd</sup> runs, the difference in temperature between the two thermocouples is much higher than in the 1<sup>st</sup> run, i.e., up to 800 K it is below 100 K, but at higher temperatures above 1100 K it can deviate by as much as 150 K. (Fig. 3(B)). In the 3<sup>rd</sup> run, the gap between the temperature recorded by the thermocouple probes and temperature estimated from known thermal EoS differs by as much 300 K, depending on the standard used for the temperature estimate. However, the temperature difference of the thermocouple located on the diamond of the cBN seat side is always no higher than +/-35 K below 800 K and +75 above 800 K in comparison to the one mounted on the side with the WC seat at the highest temperature. One can also observe that on the cBN side the temperature difference increases significantly above 1000 K.

There is a slight difference between the temperature estimate using the EoS of NaCl

and that of Au in the mixed phase experiments (Runs 2 and 3 displayed in Fig. 3), but the estimated temperature from the thermocouple on the cBN side is always lower than that on the WC side, as in run 1. In the case of NaCl, the temperature difference between the estimates in the sample chamber and the thermocouple fluctuate by +/- 35 K, while the difference between the sample chamber and the thermocouple on the WC side increase constantly until reaching a maximum of + 170 K at 1100 K. When using Au as a standard for estimating the temperature we find a similar behavior, except that the temperature differences are much larger, i.e. the temperature recorded by the thermocouple on the cBN side is lower than the temperature estimated from the Au EoS. At the same time the difference based on the temperature recorded on the WC side is much higher and reaches a value of as high as 300 K at 1300 K. We attribute the difference between the temperature estimates for NaCl and Au in the mixture to the fact that the Au foil was touching the diamond mounted on the WC side thus sensing the higher temperatures from this side.

The above observations indicate that in the original design, consisting of a small conical cBN seat and a large-slotted WC seat, the temperatures of the diamond on the cBN side is always lower than the temperature of the diamond on the WC seat, likely because of the higher thermal conductivity of the cBN seat that allows more heat to dissipate into the DAC body. Based on the calibration with an internal standard (NaCl or NaCl and Au mixture), the temperature of the sample is closest to that recorded on the cBN side. This means that there is a temperature gradient between the position of thermocouple on the diamond on the WC seat and the one on the cBN as described in Fig. 4. The distinct thermal conductivities of the seat materials resulted in a more efficient diversion of heat from the diamond tip on the cubic boron nitride (cBN) side compared to the tungsten carbide (WC) side. The gradient between the diamonds on the WC and the cBN seats becomes steeper at higher temperatures, when the heat

loss is more significant on the cBN seated side. This also explains the increased heating power consumption at higher temperatures. There may be a minimal temperature gradient within the sample itself, while the more significant gradient arises from the fact that the thermocouples are positioned on the diamonds located on different seats. Nevertheless, the difference to the temperature of the sample itself does not change significantly, so that one can always rely on the lowest recorded temperature (recorded with the thermocouple on the cBN side) being closest to the actual sample temperature. The temperature difference between the sample temperature and the recorded thermocouple temperature attached to the diamond of the cBN seated side in the three calibration runs of GRHDAC indicates that the maximum differences between the recorded temperature of the thermocouple attached to the cBN side and the sample is +/- 35 K until 800 K and above this + 90 K, +75 K, and +60 K, respectively (Fig. 2(d) and 3(d)). Based on the maximum temperature differences, we conservatively estimated that the overall temperature uncertainty of the GRHDAC with the cBN and WC seats combination to be +/- 35 until 800 K and above + 90 K.

In order to reduce the temperature gradient across the diamonds and the sample area, tests were performed employing different seat materials and the combination thereof. Fig. 5(a) shows the results of the temperature calibration using seat combination of ZrO<sub>2</sub>(slit)-WC(BA) and of ZrO<sub>2</sub> (slit)-ZrO<sub>2</sub> (BA). The most homogenous temperature distribution was achieved when using both the slotted and the BA type seats consisting of ZrO<sub>2</sub> (which has a very low thermal conductivity) where the temperature difference between the thermocouple probes on the diamonds was less than 30 K at 1300 K and less than - 40 K to the sample up to 900 K (Fig. 5(a) and 5(b)). Above 900 K, the diffraction peak of Au shifted to higher 2θ values indicating pressurization of sample, so that it was not possible to estimate the real sample temperature from Au diffraction peaks alone. When combining a BA seat consisting of WC with a slotted

ZrO<sub>2</sub> seat, thermal gradient between the two thermocouples probing diamond temperature was much steeper in comparison to the combination of the slotted WC with the conical cBN seat. The thermal efficiency when using ZrO<sub>2</sub> seats on both sides was also significantly improved compared to when employing WC or cBN seat on either side. (Fig. 5(c)). At temperatures of about 1100 K, power consumption was cut by half when using ZrO<sub>2</sub> seat on both sides in comparison to other combination of seat materials. It has also become clear that the heating efficiency based on the electrical input power is relatively constant when the same combination of seat materials is used. Therefore, deployment of ZrO<sub>2</sub> seats on both sides is best for achieving precise sample temperature and pressure from the EoS of combined pressure and temperature standards during *in-situ* high pressure and temperature X-ray diffraction measurements using GRHDAC. Unfortunately, the BA type seats made of ZrO<sub>2</sub> are only stable up to 20 GPa. In summary, the overall temperature uncertainty when using the combination of a WC and cBN seat is  $\pm 35$  K until 800 K and above  $+ 90$  K while that for the ZrO<sub>2</sub> seats (regardless of the combination of seat shapes) is  $- 55$  K up to the highest temperatures of 900 K.

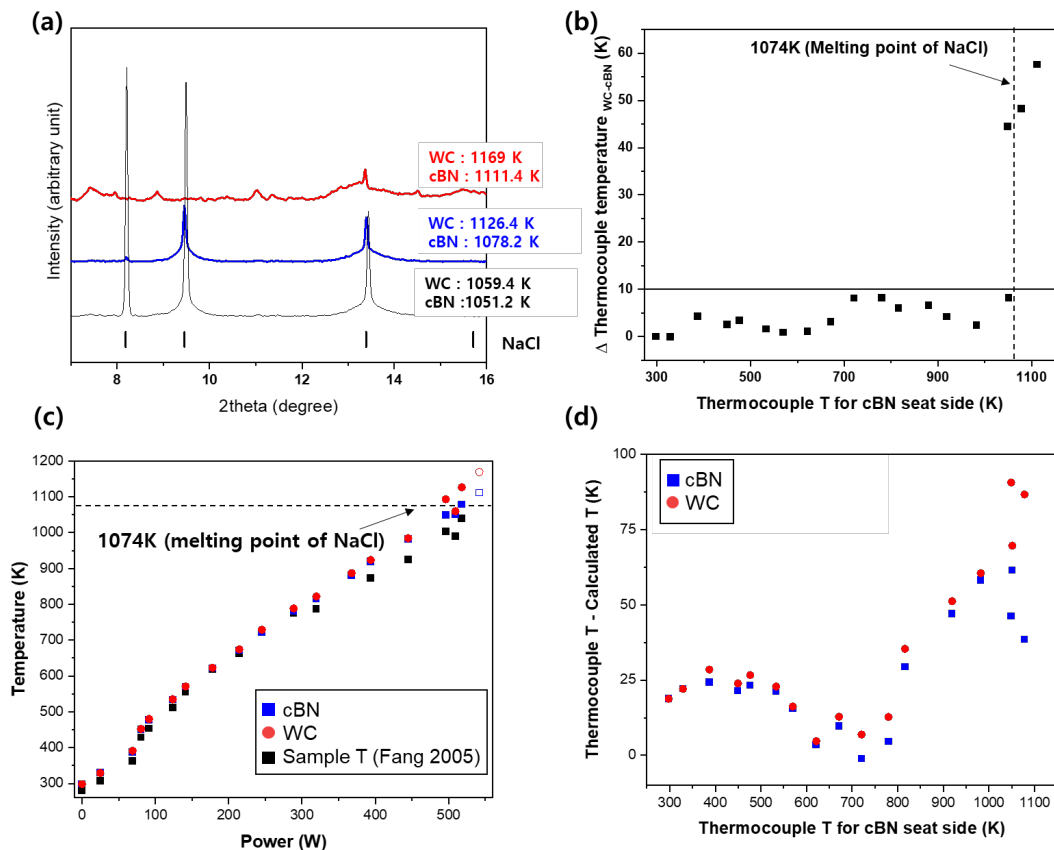


**Fig. 2** (a) X-ray diffraction patterns before (blue) and after (red) melting of pure NaCl in 1<sup>st</sup> calibration run. Tick marks at the bottom of the X-ray diffraction patterns represent the position of Bragg reflections of NaCl. (b) Difference of recorded temperature between both thermocouples. (c) Plot of temperature recorded by the thermocouples and sample temperature using the thermal expansion coefficient from Fang (2005) as a function of power.<sup>21</sup> Open shapes on the right-hand side show the recorded temperature after melting of NaCl. (d) The figure depicts the difference between the recorded thermocouple and sample temperature, as a function of the thermocouple temperature attached on the cBN seat side.

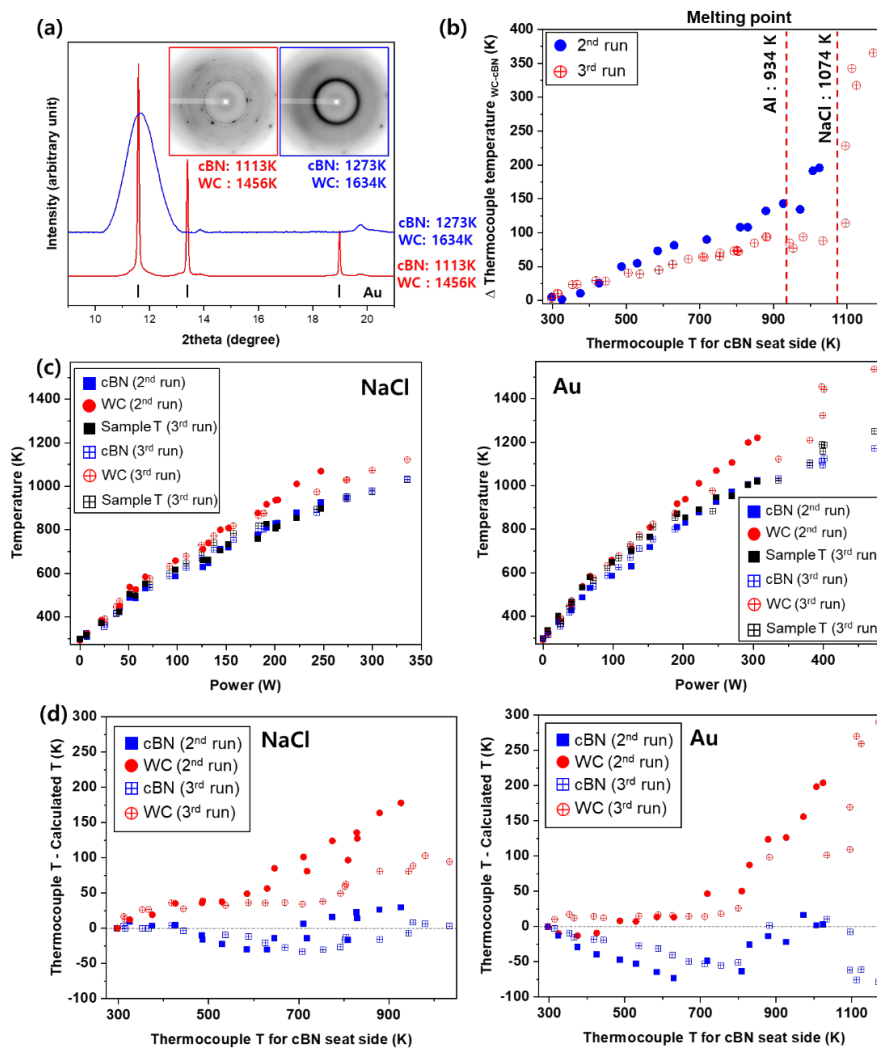


**Fig. 3.** (a) Selected diffraction images and integrated diffraction patterns before and after melting of Au in the 2<sup>nd</sup> calibration run. (b) The temperature difference between the two thermocouples attached to the diamonds. (c) The correlation of power vs. temperature in the 2<sup>nd</sup> and 3<sup>rd</sup> calibration runs based on the temperatures measured by the thermocouples and the temperature calculated using the thermal expansion coefficient for NaCl from Fang (2005) and those for Au from Pamato et al. (2018).<sup>21-22</sup> (d) The differences between the recorded thermocouple temperature and the calculated temperature based on the thermal expansion coefficients of NaCl and Au, as a function of the measured thermocouple temperature for the cBN seat side.

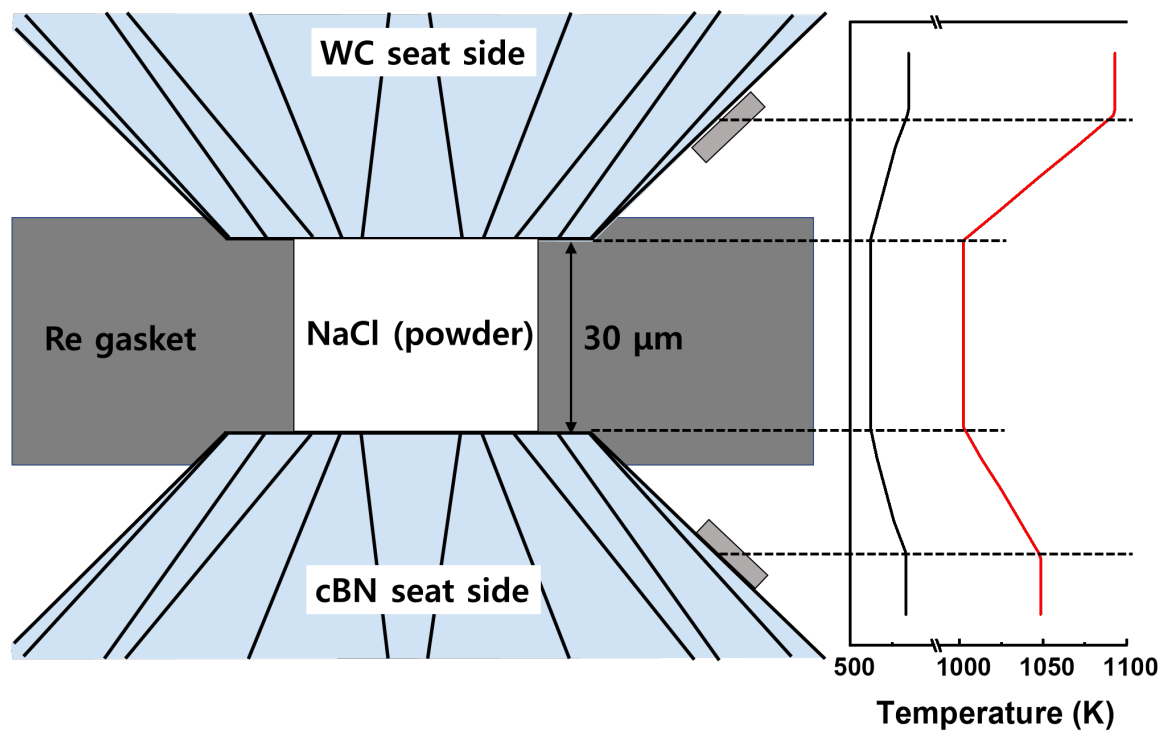


**Fig. 4.** Schematic showing the temperature distribution between both diamonds during the 1<sup>st</sup> calibration run. The black and red lines denote the temperature distribution at the sample temperature of 512 and 1002 K, respectively.

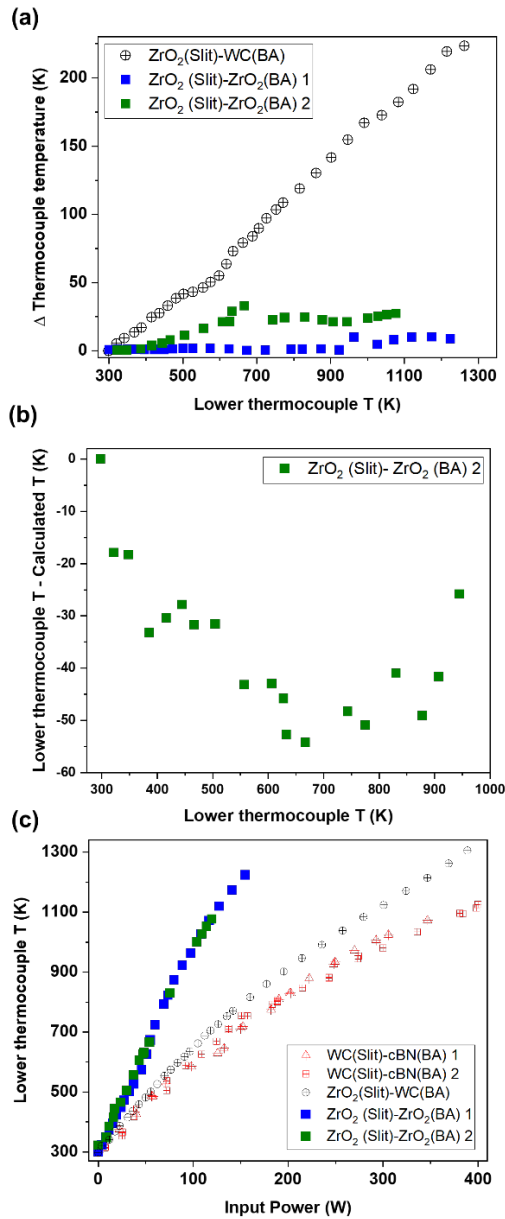


**Fig. 5.** (a) Probed temperature differences between two thermocouples attached to the pavilions of diamonds with different seat combinations. Open black circles with crosses represent the result from combining a BA seat comprised of WC with a slotted ZrO<sub>2</sub> seat. The rest of the plots originate from experimental results using ZrO<sub>2</sub> seats on both sides (Blue and Green squares). (b) Temperature differences between the temperature recorded by the thermocouples and the sample derived from the EoS of Au.<sup>22</sup> (c) Heating efficiency of different seat combinations as a function of power consumption.

## Applications of GRHDAC

### A. Stability of hydrous minerals under subduction zone conditions

The stability of subducting hydrous minerals is critical for understanding the H<sub>2</sub>O transport process of the Earth's interior. The GRHDAC has been useful for generating simultaneous high-pressure and -temperature conditions encountered in the subduction zone. Through high-pressure and -temperature experiment using the GRHDAC combined with X-ray diffraction, the stability field and phase transition of hydrous minerals under subduction zone conditions can be studied. Fig. 6 shows the pressure and temperature path of the high-pressure and -temperature experiment for the hydrous mineral, glaucophane ( $\text{Na}_{2.09}(\text{Mg}_{2.7}\text{Fe}_{0.8}\text{Al}_{1.6})\text{Si}_{17.97}\text{O}_{22}(\text{OH})_2$ ), following a cold subduction geotherm using the GRHDAC. Au powder with a purity of 99.9 % (Sigma Aldrich, product no. 326585) was loaded as a pressure marker together with a powdered sample of glaucophane in the GRHDAC. Sample pressure was determined using the thermal equation of state of Au from Anderson (1989).<sup>24</sup> In order to realize a cold subduction environment, the sample was mixed with 4 wt.% of H<sub>2</sub>O<sup>25</sup> and loaded in the GRHDAC. In high-pressure and -temperature experiment of the glaucophane using GRHDAC, the pressure and temperature condition followed the geotherm models predicted for Tonga or North Antilles as described by Syracuse et al. (2010).<sup>26</sup> As the temperature increased to 850 K, a sample pressure increase was observed. Considering the reported thermo elasticity of glaucophane, the maximum thermal pressure that glaucophane can experience was estimated to be approximately 1 GPa.<sup>27,28</sup> Thus, the observed pressure increases to 3 GPa at 850 K cannot entirely be explained by thermal pressure. Additional pressurization during the heating is most probably due to the thermal expansion of components of the GRHDAC heated in the vicinity of the diamonds. To determine the high-temperature bulk modulus of glaucophane, isothermal X-ray diffraction data were collected at 850 K by

increasing the pressure through the gas membrane up to 6.3(3) GPa. At 7.8(3) GPa and 1030 K, which is equivalent to ca. 250 km depth in the modeled geotherm, X-ray diffraction pattern confirmed the dehydration breakdown of glaucophane into jadeite ( $2\text{NaAlSi}_2\text{O}_6$ ), enstatite ( $1.5(\text{Mg}_{1-x}\text{Fe}_x)_2\text{Si}_2\text{O}_6$ ), coesite ( $\text{SiO}_2$ ), and  $\text{H}_2\text{O}$  fluid. When the compressibility of glaucophane at ambient temperatures is compared with that at high-temperature, we noted a suppression of the elastic anisotropy of glaucophane at high-temperature, which might contribute to the observed seismic anisotropy observed at the corresponding depth in the Tonga subduction zone. More details about this study may be found in Bang et al. (2021).<sup>15</sup>

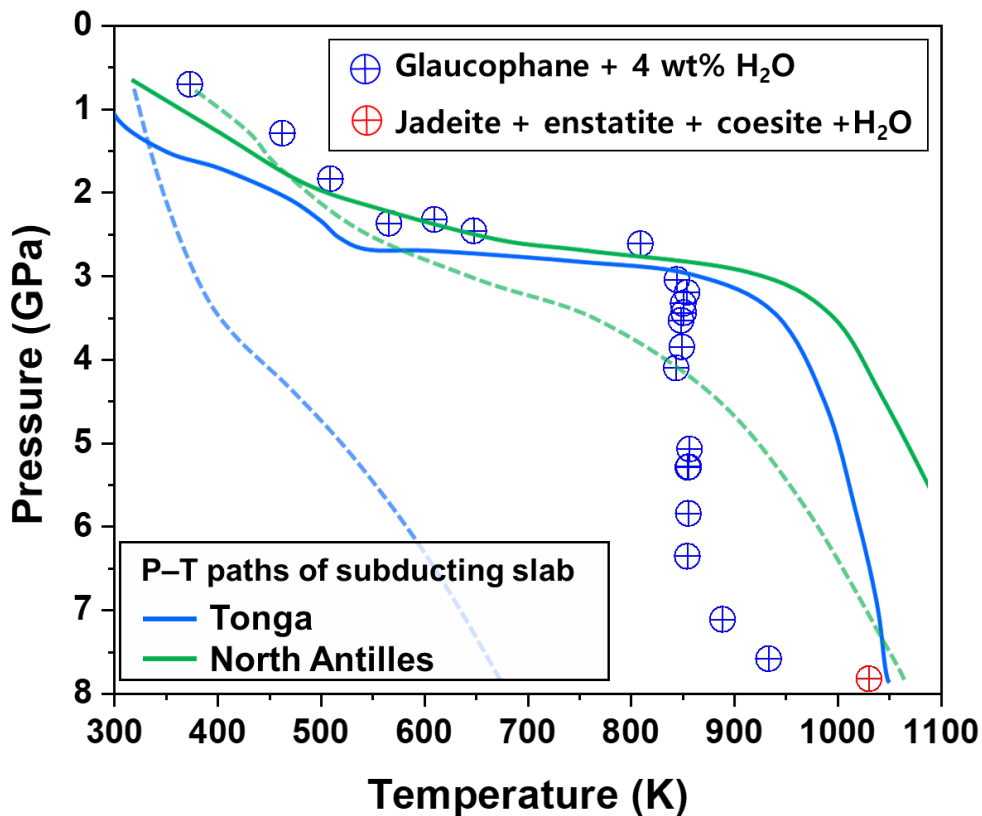


**Fig. 6.** Experimental pressure and temperature path explored in the study of glaucophane in the GRHDAC. Lines represent the pressure and temperature condition of the Tonga (Blue) and North Antilles (Green) subduction zone from Syracuse et al. (2010).<sup>26</sup> Dotted lines indicate the geotherms at Moho while continuous lines are representing the corresponding slab surface.

## B. Application of the GRHDAC in single crystal diffraction

*In-situ* single-crystal X-ray diffraction experiments at combined high-temperature and high-pressure conditions (HPHT-SC-XRD) may provide data on the intrinsic structural stability of investigated samples, allowing not only the determination of  $P$ - $T$ - $V$  equations of state, but also the description of the structural mechanisms that govern, at the atomic scale, the bulk ( $P$ ,  $T$ )-behavior of the mineral (or synthetic compound) under investigation and its physical properties in general. These capabilities, made available by the use of the GRHDAC, are particularly relevant in tracking the occurrence and determining the critical  $T/P$  of phase transitions and corresponding structural evolutions.

Here we here report, as an example of *in-situ* HPHT-SC-XRD in the GRHDAC, the case study on scapolite. Scapolite is a group of open-framework aluminosilicates with general formula  $M_4T_{12}O_{24}A$ , where  $M$  are monovalent or divalent cations (usually Na, Ca and minor K),  $T$  are trivalent or tetravalent cations (mostly Al and Si) in tetrahedral coordination, and  $A$  are anions such as Cl, CO<sub>3</sub> and SO<sub>4</sub>. Three mineral end members are recognized: marialite (Na<sub>4</sub>Al<sub>3</sub>Si<sub>9</sub>O<sub>24</sub>Cl), meionite (Ca<sub>4</sub>A<sub>16</sub>Si<sub>6</sub>O<sub>24</sub>CO<sub>3</sub>), and silvialite (Ca<sub>4</sub>A<sub>16</sub>Si<sub>6</sub>O<sub>24</sub>SO<sub>4</sub>) even though most of the natural samples are of a given intermediate composition<sup>29</sup>. They are common rock-forming or accessory minerals, mainly encountered in metamorphic rocks of the amphibolite or granulite facies<sup>30-32</sup>. It is therefore of geological relevance to understand the behavior of scapolite-group members at non-ambient  $T$  and  $P$  conditions.

In a previous study on the compressional behavior at room temperature of an intermediate member of the scapolite solid solution, (Na<sub>1.86</sub>Ca<sub>1.86</sub>K<sub>0.23</sub>Fe<sub>0.01</sub>)(Al<sub>4.36</sub>Si<sub>7.64</sub>)O<sub>24</sub>[Cl<sub>0.48</sub>(CO<sub>3</sub>)<sub>0.48</sub>(SO<sub>4</sub>)<sub>0.01</sub>], Lotti et al. (2018)<sup>33</sup> reported the occurrence of a single-crystal to single-crystal phase transition from the tetragonal  $I4/m$  to the triclinic  $II$  space group, bracketed between 9.23 and 9.87 GPa. In order to investigate if the

same phase transition would occur at higher temperature, an *in-situ* HPHT-SC-XRD experiment has been performed at beamline P02.2 at PETRA-III, DESY (Hamburg, Germany) using the GRHDAC. A single crystal fragment of the same sample studied by Lotti et al. (2018)<sup>33</sup> was loaded in the *P*-chamber (0.2 mm in diameter) obtained by spark-erosion of a rhenium gasket previously pre-indented to *ca.* 0.050 mm, along with ruby spheres and gold powder as pressure calibrants; silicone oil was used as the *P*-transmitting medium. Pressure was initially estimated using the ruby fluorescence shift<sup>34</sup> and at HPHT using the *P-T-V* equation of state of gold<sup>24</sup>, monitoring the shifts of the (111), (200) and (220) diffraction lines. A monochromatic X-ray beam (42.7 keV,  $\lambda = 0.2904 \text{ \AA}$ ) was used and the diffraction patterns were collected on a Perkin-Elmer XRD 1621 flat panel detector. For each dataset, the following data collection strategy was adopted: a step-wise  $\omega$ -scan from  $-25^\circ$  to  $+25^\circ$  (which allowed for a  $\sim 55\%$  completeness), with  $0.5^\circ$  step-scan and 1 second exposure time per frame. The instrumental model was calibrated using a crystal of ortho-enstatite [(Mg<sub>1.93</sub>, Fe<sub>0.06</sub>)(Si<sub>1.93</sub>,Al<sub>0.06</sub>)O<sub>6</sub>, (Space group, *Pbca*,  $a = 18.2391 (3)$ ,  $b = 8.8117 (2)$ ,  $c = 5.18320 (10)$   $\text{\AA}$ ]. Data were collected using an in-house script and then converted to the “Esperanto” format in order to be processed in CrysAlisPro<sup>35-36</sup> for the indexing of the X-ray diffraction peaks, unit-cell refinements and intensity data reduction (corrected for Lorentz-polarization effects). The semi-empirical ABSPACK routine, implemented in CrysAlisPro, was applied to correct for absorption effects of the DAC components. Structure refinements were performed using JANA2006<sup>37</sup> starting from the model (and applying the same restrictions and assumptions) reported by Lotti et al. (2018)<sup>33</sup> for the refinements based on the high-pressure datasets. Three data collections at ambient-*T* were performed from 0.0001 up to 1.42 GPa and then the temperature was increased up to 923 K with data collections every 100 K. As described in section A, pressure also increased at this stage. At 923 K, an isothermal compressional ramp

from 8.98 up to 16.16 GPa was performed with ten dataset collections (Table 1). The tetragonal  $I4/m$  structural model of scapolite has been successfully determined up to 10.30 GPa at 923 K, whereas, at 10.71 GPa, the triclinic  $I-1$  structure already described by Lotti et al. (2018)<sup>33</sup> was detected. The triclinic unit-cell parameters were indexed up to the highest pressure investigated of 16.16 GPa, even though observing a continuous and significant decrease in the intensity of the diffraction peaks with pressure. As shown in Fig. 7, based on the data reported here and those previously published<sup>33</sup>, it appears that the phase transition is significantly more controlled by pressure rather than by thermal excitation. Relevant structural parameters from the selected refinements are reported in Table 2. A comparison with the structural data reported from the isothermal compression at 298 K<sup>33</sup> shows that the same dominant structural mechanisms mainly controlled by pressure occur, with the anti-cooperative rotation of the 4-membered rings of tetrahedra in the  $(hk0)$  plane, which induces a compression of the channels along the shorter axis with related increase in ellipticity (Fig. 7 and Table 2). It is the dominant one. It is worth note that the structure refinements based on the HTHP data also suggest that the phase transition is likely induced by the saturation in the compressional trend of selected interatomic bonds involving the  $M$  cations (Table 3; see also Lotti et al. 2018)<sup>33</sup>, demonstrating the potential use of this experimental setup for thorough structural characterization and understanding of phase transitions at both high- $T$  and high- $P$  conditions.

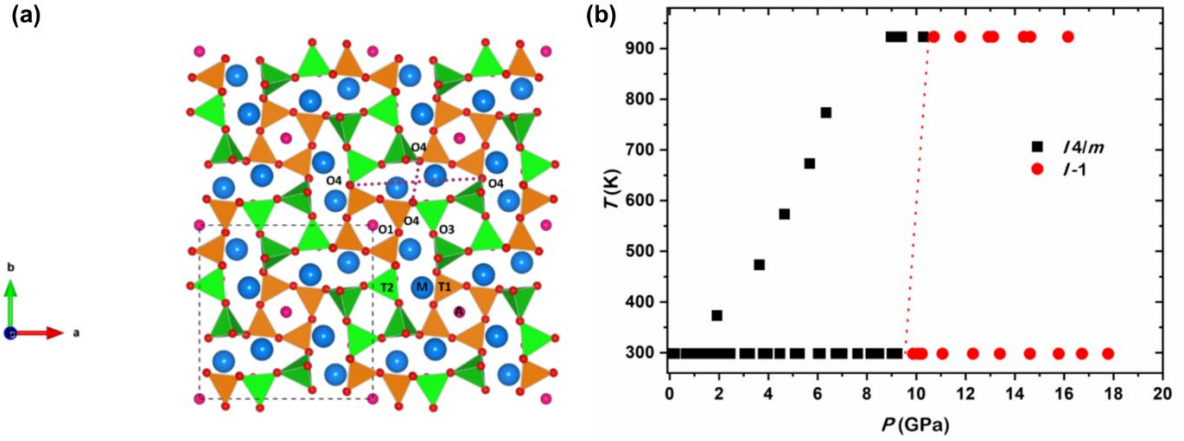


**Fig. 7. (a)** The crystal structure of scapolite viewed along the  $c$ -axis. Orange and green tetrahedra represent the independent  $T1$  and  $T2$  sites, respectively, whereas red, blue and purple spheres refer respectively to the oxygen, cations ( $M$ ) and anions ( $A$ ) positions. **(b)** Experimental phase diagram of tetragonal and triclinic scapolite at varying  $T$  and  $P$  conditions (based on data of Lotti et al., 2018<sup>33</sup>, and those reported in this manuscript).

**Table 1.** Unit-cell parameters of the tetragonal and triclinic polymorphs of scapolite at different temperature and pressure.

$T$ (K)	$P$ (GPa)	$a$ (Å)	$b$ (Å)	$c$ (Å)	$\alpha$ (°)	$\beta$ (°)	$\gamma$ (°)	$V$ (Å <sup>3</sup> )
298*	0.0001*	12.1136(3)		7.5588(3)	90	90	90	1109.2(1)
298	1.27	12.0273(5)		7.5228(4)	90	90	90	1088.2(1)
298	1.42	12.0235(4)		7.514(2)	90	90	90	1086.3(2)
373	1.92	11.9869(8)		7.5117(7)	90	90	90	1079.3(1)
473	3.64	11.9497(13)		7.4733(14)	90	90	90	1067.1(3)
573	4.67	11.8578(5)		7.4491(4)	90	90	90	1047.4(1)
673	5.68	11.8541(5)		7.4422(4)	90	90	90	1045.8(1)
773	6.35	11.8371(4)		7.4273(4)	90	90	90	1040.7(1)
923	8.98	11.7378(5)		7.364(2)	90	90	90	1014.6(3)
923	9.41	11.7280(5)		7.311(2)	90	90	90	1005.6(3)
923	10.30	11.7206(11)		7.289(5)	90	90	90	1001.3(6)
923	10.71	11.714(4)	11.556(5)	7.319(3)	88.05(12)	89.88(6)	89.67(5)	990(2)
923	11.78	11.673(5)	11.573(11)	7.132(6)	86.86(7)	90.57(6)	89.72(6)	962(1)
923	12.93	11.684(5)	11.503(14)	7.164(7)	86.51(9)	90.26(6)	89.62(6)	961(1)
923	13.11	11.638(7)	11.507(11)	7.077(6)	86.19(7)	90.89(8)	89.51(7)	946(1)
923	14.36	11.619(9)	11.485(13)	7.103(8)	86.22(9)	90.94(10)	89.44(9)	946(2)
923	14.63	11.616(11)	11.40(2)	6.690(10)	85.05(12)	91.38(11)	88.97(10)	917(2)
923	16.16	11.59(2)	11.32(3)	6.83(2)	83.6(3)	91.7(2)	88.9(2)	889(4)

\* Crystal in the DAC without  $P$ -medium (prior to assembly in the GRHDAC)

**Table 2.** Angles ( $^{\circ}$ ), distances ( $\text{\AA}$ ) and volumes ( $\text{\AA}^3$ ) from selected refinements of tetragonal scapolite at different temperatures and pressures. The O4-O4 distances refer to the diagonals of the  $8mR_{hk0}$  shown in Figure 7a.

<i>T</i> (K)	<i>P</i> (GPa)	T1-O1- T1	T2-O2- T2	T2-O3- T2	T1-O4- T2	O1-O4- O3	$8mR_{hk0}$ O4-O4	$8mR_{hk0}$ O4-O4	$8mR_{hk0}$ $\epsilon^{**}$	$V(M)^{***}$
298*	0.0001*	157.8(3)	139.54(4)	146.3(2)	137.1(2)	93.34(9)	3.119(7)	9.335(8)	0.3341(10)	18.82(8)
298	1.27	157.7(3)	139.25(4)	146.0(2)	136.6(2)	92.43(9)	3.045(7)	9.323(8)	0.3266(10)	18.34(8)
273	1.92	157.5(4)	139.77(7)	146.5(3)	136.3(2)	92.06(10)	3.017(8)	9.313(8)	0.3240(11)	18.27(8)
573	4.67	157.6(5)	138.55(6)	145.4(4)	135.3(3)	90.90(13)	2.910(10)	9.290(10)	0.3132(14)	17.41(10)
773	6.35	157.6(5)	138.17(6)	144.5(4)	135.3(3)	90.6(2)	2.899(12)	9.275(12)	0.313(2)	17.37(12)
923	8.48	158.3(5)	137.8(2)	145.1(3)	135.8(5)	90.20(14)	2.846(12)	9.236(10)	0.308(2)	17.1(2)
923	9.41	158.0(5)	137.4(2)	144.6(3)	135.6(5)	90.1(2)	2.84(2)	9.230(12)	0.307(2)	17.0(2)
923	10.30	157.5(7)	136.7(3)	145.1(6)	134.1(7)	89.7(3)	2.78(3)	9.28(2)	0.300(3)	16.8(4)

\* Crystal in the DAC without *P*-medium; \*\* defined as ( $8mR_{hk0}$  O4-O4 short)/(  $8mR_{hk0}$  O4-O4 long); \*\*\* volume of the *M* cation coordination polyhedron calculated using the tools implemented in VESTA3 (Momma and Izumi 2011)<sup>38</sup>

**Table 3.** Interatomic bonds ( $\text{\AA}$ ) of tetragonal scapolite involving the *M* cations coordination environment from selected structure refinements at different T and P.

<i>T</i> (K)	<i>P</i> (GPa)	<i>M</i> -O2	<i>M</i> -O3 (x 2)	<i>M</i> -O4' (x 2)	<i>M</i> -O4'' (x 2)	<i>M</i> -A
298*	0.0001*	2.347(4)	2.516(3)	2.765(3)	2.888(3)	3.108(2)
298	1.27	2.347(5)	2.501(4)	2.746(4)	2.891(3)	3.116(2)
373	1.92	2.325(5)	2.481(4)	2.732(4)	2.845(4)	3.059(2)
573	4.67	2.296(7)	2.432(5)	2.693(5)	2.798(4)	3.021(2)
773	6.35	2.302(8)	2.418(6)	2.707(6)	2.788(5)	2.994(4)
923	8.48	2.297(9)	2.406(8)	2.689(7)	2.772(10)	2.943(3)
923	9.41	2.304(10)	2.394(9)	2.698(8)	2.751(11)	2.927(4)
923	10.30	2.287(14)	2.397(16)	2.683(13)	2.734(20)	2.920(4)

### C. Xe retention in deep hydrous silicates

Atmospheric Xe is recycled at depth via subduction,<sup>39</sup> and potentially carried in cyclo-silicates due to their cage and channels like structures.<sup>40</sup> Xenon retention in compressed SiO<sub>2</sub> quartz and (Mg,Fe)<sub>2</sub>SiO<sub>4</sub> olivine occurs through substitution of Xe with Si at high T, inducing the formation of Xe-O covalent bonds.<sup>41-44</sup> To investigate Xe retention in more complex naturally relevant systems, we have worked on the Xe-KNaAlSi<sub>3</sub>O<sub>8</sub>-H<sub>2</sub>O system up to 9.7 GPa and 1473 K to target the P-T stability field of K-cymrite, the high P form of K-feldspar. Xenon is a very heavy element, hence strongly contributes to the X-ray diffracted signal. However, only 0.9 Xe wt% is retained in the crystalline structure, hence it is essential to optimize the quality of the X-ray diffraction patterns for accurate crystal structure refinement and proper identification of Xe crystal-chemistry. For that purpose, sample was loaded as a glass previously synthesised in a one atmosphere furnace, and further hydrated and doped with Xe using a piston-cylinder press.<sup>45</sup> Indeed, when the glass transition is crossed upon heating, it results in a powder pattern with very good ring statistics (see Fig.8).

Such quality would not be obtained during laser heating in the DAC. Differences in intensity between plain and Xe-doped K-cymrite are small but still evident on the first four diffraction peaks (Fig.9), including disappearance of the lowest angle diffraction peak. Amongst the different crystallographic sites tested for Xe, only one matches the X-ray diffraction data. It does not correspond to rings site, as expected for other volatiles such as N<sub>2</sub>, Ar, or H<sub>2</sub>O,<sup>46</sup> but instead Xe sits in between sheets of [SiO<sub>4</sub>]<sup>4-</sup> tetrahedra, surrounded by six oxygen atoms in the same configuration as [XeO<sub>6</sub>]<sup>4-</sup> perxenate octahedra in K<sub>4</sub>Xe<sub>3</sub>O<sub>12</sub> perovskite.<sup>47</sup> However, a precise structure refinement will require collecting additional data with a higher Xe content. Indeed, the Xe content in recovered cymrite equals that in the starting glass, and no Xe bubbles were observed, attesting that 0.9wt% is below the Xe solubility for

K-cymrite.

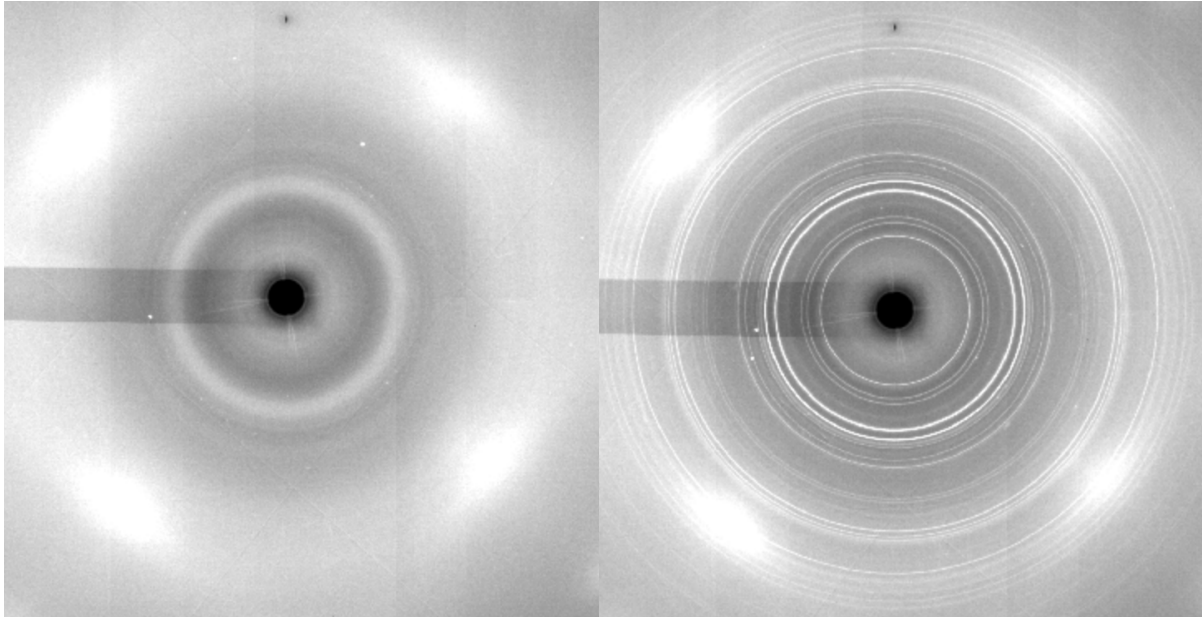


**Fig. 8.** 2-D X-ray diffraction signal of (left) glass sample (hydrous feldspar glass doped with 0.9 wt%Xe at 9.7 GPa GPa and 880°C), and (right) re-crystallized pattern at 9.7 GPa and 1080°C. White shadows are diamond Bragg peaks from the anvils.

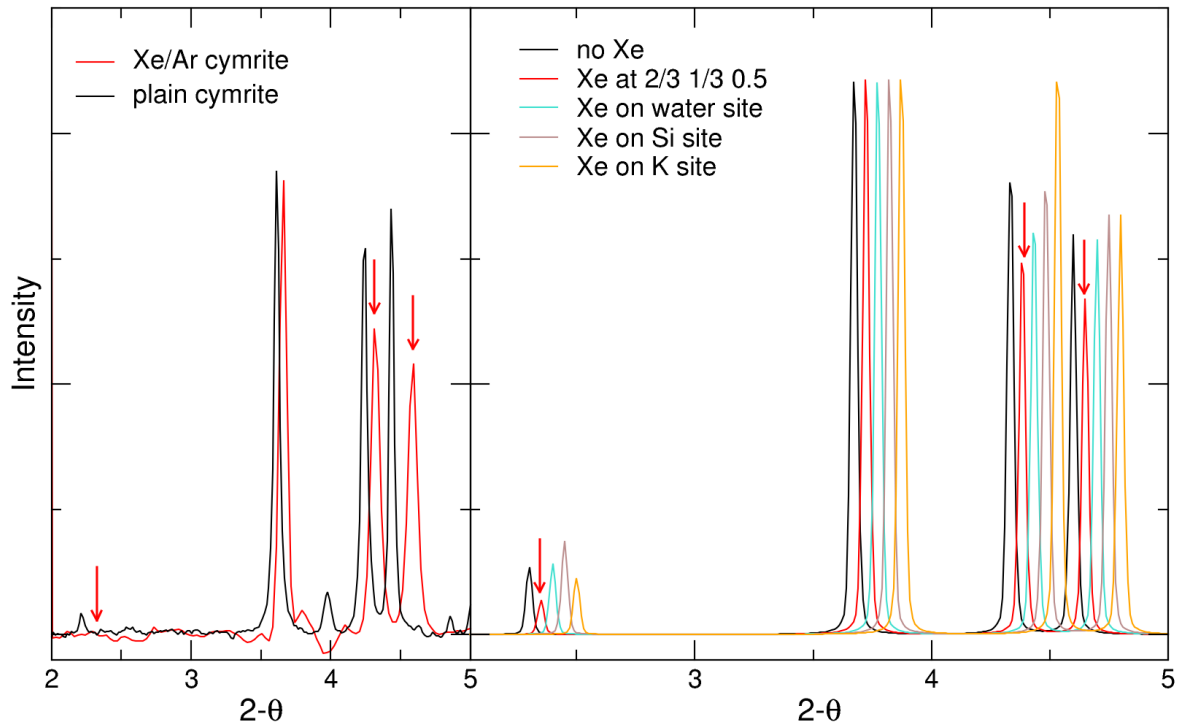


**Fig. 9.** (Left) Integrated diffraction signal of Xe-doped and plain K-cymrite after recrystallization from glass; the arrows point to the peaks which intensity decreases in the presence of Xe in the crystalline structure. (Right) Expected X-ray diffraction signal for K-cymrite without Xe and with Xe on different crystallographic sites. Note that coloured diffractograms are shifted horizontally to visualize intensity variations.

## Outlook

Future work will focus on using a slotted and a conical  $\text{ZrO}_2$  seat for powder diffraction studies, in order to reach higher pressures at simultaneous high-temperatures and to overcome the 20 GPa pressure limit encountered when using the BA type  $\text{ZrO}_2$  seats. With this seat configuration, sample access to reciprocal space can only be reached when inverted the vacuum chamber so that slotted  $\text{ZrO}_2$  seat will be located on the downstream side. Furthermore,

fluorescence measurement of  $\text{SrB}_4\text{O}_7:\text{Sm}^{2+}$  will be implemented to estimate the pressure more precisely up to  $\sim 900$  K, since the  $\text{SrB}_4\text{O}_7:\text{Sm}^{2+}$  fluorescence lines are relatively insensitive to temperatures<sup>48-49</sup>. This will require reconfiguration of the online fluorescence microscope at P02.2 that is currently configured to monitor the sample chamber only from the downstream side.

## **Conclusion**

We present the calibration of the 4-pin type GRHDAC based on X-ray diffraction measurements of materials with well-characterized melting points, such as NaCl, and Au, up to 1500 K at ambient pressure. Moreover, we demonstrated good heating capability and reproducibility of GRHDAC when comparing EoS temperature estimates based on synchrotron X-ray diffraction measurements of internal standards with thermocouple measurements. The differences between the temperature recorded by thermocouples placed on the diamond mounted on a cBN seat and the temperature derived from EoS of Au and NaCl standards were within 75 K below 1300 K. Significant improvement of the temperature stability can be achieved when employing  $\text{ZrO}_2$  type seat. As such, the GRHDAC presented in this paper enables access to simultaneous temperature and pressure regimes that is not possible to reach using the infrared laser heated DAC. Further development of the GRHDAC technique would help to establish high precision EoS and phase stability studies in a wide range of pressure and temperature conditions and in particular those where the laser heating experiment may fail.

## Acknowledgement

H.H. thanks for the funding of this work has been provided by the Alexander von Humboldt Foundation, Germany. We acknowledge DESY (Hamburg, Germany), a member of the Helmholtz Association HGF, for the provision of experimental facilities. Parts of this research were carried out at PETRA III beamline P02.2. Beamtime was allocated for proposal II-20210012 and II-20180596. We also acknowledge the scientific exchange and support of the Centre for Molecular Water Science (CMWS). This work was supported by GIST Research Institute (GRI) IERI grant funded by the GIST in 2023. Y.L. thanks the support by the Leader Researcher program (NRF-2018R1A3B1052042) of the Korean Ministry of Science and ICT. Part of the work was performed under the auspices of the U.S. Department of Energy by Lawrence Livermore National Laboratory under Contract No. DE-AC52-07NA27344. The authors thank tow anonymous reviewers for the critical evaluation of the manuscript and N. Giordano for editing the manuscript for language and helpful discussion.

## Reference

1. T. S. Duffy, Rep. Prog. Phys. **68**(8), 1811 (2005)
2. J. P. S. Walsh and D. E. Freedman, Accounts Chem. Res. **51**(6), 1315-1323 (2018)
3. X. Wang and X. Liu, Inorg. Chem. Front. **7**, 2890-2908 (2020)
4. S. Anzellini and S. Boccato, Crystals **10**, 459 (2020)
5. T. Kunimoto, M. Nishi, and T. Irifune, “High-pressure generation to 150 GPa in multianvil apparatus using the 6-8-2 system with nano-polycrystalline diamond anvils” *In: Japan Geoscience Union - American Geophysical Union Joint Meeting 2020* (2020)
6. H.-P. Liermann “Chapter 10. X-Ray Diffraction at Extreme Conditions: Today and Tomorrow” In O. H. Seeck and B. M. Murphy “X-Ray Diffraction: Modern Experimental Techniques” pp 255-314, Pan Stanford Publishing Pte Ltd (2015)

7. B. J. Heinen, J. W. E. Drewitt, M. J. Walter, C. Clapham, F. Qin, A. K. Kleppe, and O. T. Lord, *Rev. Sci. Instrum.* **92**(6), 063904 (2021)
8. N. Dubrovinskaia and L. Dubrovinsky, *Rev. Sci. Instrum.* **74**(7), 3433-3437 (2003)
9. C.-S. Zha, K. Mibe, W. A. Bassett, O. Tschauner, H.-K. Mao, and R. J. Hemley, *J. Appl. Phys.* **103**, 054908 (2008)
10. C.-S. Zha and W. A. Bassett, *Rev. Sci. Instrum.* **74**, 1255 (2003)
11. T. Komabayashi, Y. Fei, Y. Meng, and V. Prakapenka, *Earth Planet. Sci. Lett.* **282**, 252-257 (2009)
12. G. Shen, H.-P. Liermann, S. Sinogeikin, W. Yang, X. Hong, C.-S. Yoo, and H. Cynn, *Proc. Natl. Acad. Sci. U. S. A.* **104**(37), 14576-14579 (2007)
13. C. Sanloup, R. J. Hemley, and H.-K. Mao, *Geophys. Res. Lett.* **29**(18), 1883 (2002)
14. H. Hwang, D. Seoung, Y. Lee, Z. Liu, H.-P. Liermann, H. Cynn, T. Vogt, C.-C. Kao, and H.-K. Mao, *Nat. Geosci.* **10**, 947-953 (2017)
15. Y. Bang, H. Hwang, T. Kim, H. Cynn, Y. Park, H. Jung, C. Park, D. Popov, V. B. Prakapenka, L. Wang, H.-P. Liermann, T. Irifune, H.-K. Mao, and Y. Lee, *Nat. Commun.* **12**(1) 1-7 (2021)
16. Z. Du, L. Miyagi, G. Amulele, and K. K. M. Lee, *Rev. Sci. Instrum.* **84**, 024502 (2013)
17. A. S. J. Méndez, H. Marquardt, R. J. Husband, I. Schwark, J. Mainberger, K. Glazyrin, A. Kurnosov, C. Otzen, N. Satta, J. Bednarcik, and H.-P. Liermann, *Rev. Sci. Instrum.* **91**, 073906 (2020)
18. D. Comboni, P. Lotti, G. D. Gatta, M. Merlini, H.-P. Liermann, and D. J. Frost, *Phys. Chem. Miner.* **45**(3), 259-278 (2018)
19. C. Prescher, V. B. Prakapenka, *High Pressure Res.* **35**, 223-240 (2015)
20. J. B. Ferguson *J. Phys. Chem.* **26**(7), 626-630 (1922)
21. Z.-H. Fang, *Physica B* **357**, 433-438 (2005)
22. M. G. Pamato, I. G. Wood, D. P. Dobson, S. A. Hunt, and L. Vočadlo, *J. Appl. Crystallogr.*

- 51**, 470-480 (2018)
23. T. Iida, and R. I. L. Guthrie “The Physical Properties of Liquid Metals” Clarendon, Oxford (1988)
24. O. L. Anderson, D. G. Isaak, and S. Yamamoto, *J. Appl. Phys.* **65**, 1534–1543 (1989)
25. P. E. van Keken, B. R. Hacker, E. M. Syracuse, and G. A. Abers, *J. Geophys. Res.* **116**, B10401 (2011)
26. E. M. Syracuse, P. E. van Keken, and G. A. Abers, *Phys. Earth Planet. Inter.* **183**, 73-90 (2010)
27. D. M. Jenkins, and J.-C. Corona, *Phys. Chem. Miner.* **33**, 356-362 (2006)
28. M. D. Welch, F. Cámara, and R. Oberti, *Phys. Chem. Miner.* **38**, 321-334 (2011)
29. Y. Seto, N. Shimobayashi, A. Miyake, and M. Kitamura, *Am. Mineral.* **89**, 267-265 (2008)
30. A. J. Stoltz, *Mineral. Mag.* **51**, 719-732 (1987)
31. W. H. Oterdoom, and H-S. Wenk, *Contrib. Mineral. Petrol.* **83**, 330-341 (1983)
32. D. P. Moecher, and E. J. Essene, *Contrib. Mineral. Petrol.* **108**, 219-240 (1991)
33. P. Lotti, D. Comboni, M. Merlini, and M. Hanfland, *Phys. Chem. Miner.* **45**, 945-962 (2018)
34. H. K. Mao, J. Xu, and P. M. Bell, *J. Geophys. Res.* **91**, 4673-4676 (1986)
35. Rigaku Oxford Diffraction, “*CrysAlisPro Software system, version 1.171.41*” Rigaku Corporation, Wroclaw (2018)
36. A. Rothkirch, G. D. Gatta, M. Meyer, S. Merkel, M. Merlini, and H-P. Liermann, *J. Synchrotron Rad.* **20**, 711-720 (2013)
37. V. Petříček, V. Dušek, and L. Palatinus, *Z. Kristallogr.* **229**, 345-352 (2014)
38. K. Momma, and F. Izumi, *J. Appl. Crystallogr.* **44**, 1272-1276 (2011)
39. G. Holland, and C. J. Ballentine, *Nature* **441**, 186–91 (2006)
40. C. R. M. Jackson, S. W. Parman, S. P. Kelley, and R. F. Cooper. *Nat. Geosci.* **6**, 562–5

(2013)

41. M. I. J. Probert. *J Phys.* **22**, 025501 (2010)
42. J. Kalinowski, M. Rasanen, and R. B. Gerbe, *Phys. Chem. Chem. Phys.* **16**, 11658–61 (2014)
43. C. Crépisson, M. Blanchard, M. Lazzeri, E. Balan, and C. Sanloup, *Geochim. Cosmochim. Acta.* **222**, 146–55 (2018)
44. C. Crépisson, C. Sanloup, M. Blanchard, J. Hudspeth, K. Glazyrin, and F. Capitani. *Geochem Geophys Geosyst.* **20**, 992–1003 (2019)
45. A. Montana, Q. Guo, S. Boettcher, B. White, and M. Brearley Xe and Ar in high pressure silicate liquids. *Am. Mineral.* **78**, 1135-1142 (1993)
46. A. G. Sokol, I. Kupriyanov, Y. Seryotkin, E. Sokol, A. N. Kruk, A. A. Tomilenko, T. A. Bul'bak, and Y. Palyanov. *Gondwana Res.* **79**, 70-86 (2020)
47. S. N. Britvin, S. A. Kashtanov, S. V. Krivovichev, and N. V. Chukanov. *J. Amer. Chem. Soc.* **138**, 13838-13841 (2016)
48. A. F. Goncharov, J. M. Zaug, and J. C. Crowhurst, *J. Appl. Phys.* **97**(9), 094917 (2005)
49. F. Datchi, A. Dewaele, Y. Le Godec, and P. Loubeyre, *Phys. Rev. B* **75**, 214104 (2007)